

1 **Quantifying the driving factors of particulate matter variabilities in the Beijing-Tianjin-Hebei**
2 **and Yangtze River Delta regions from 2015 to 2022 by machine learning approach**

3 Zhongfeng Pan^{1,2}, Hao Yin^{3,*}, Zhenda Sun², Chongyang Li², Youwen Sun^{1,2,4,*}, Cheng Liu^{5,6,*}

4 ¹ Institutes of Physical Science and Information Technology, Anhui University, Hefei 230601, China;

5 ² Key Laboratory of Environmental Optics and Technology, Anhui Institute of Optics and Fine
6 Mechanics, HFIPS, Chinese Academy of Sciences, Hefei 230031, China

7 ³ School of Energy and Environment, City University of Hong Kong, Hong Kong SAR, China

8 ⁴ School of Environmental Science and Optoelectronic Technology, University of Science and
9 Technology of China, Hefei 230026, China

10 ⁵ Department of Precision Machinery and Precision Instrumentation, University of Science and
11 Technology of China, Hefei 230026, China

12 ⁶ Key Laboratory of Precision Scientific Instrumentation of Anhui Higher Education Institutes,
13 University of Science and Technology of China, Hefei 230026, China

14 Corresponding author: Hao Yin (haoyin@cityu.edu.hk); Youwen Sun (ywsun@aiofm.ac.cn); Cheng
15 Liu (chliu81@ustc.edu.cn)

16
17 **Abstract.** Accurately quantifying the relative roles of anthropogenic emissions and meteorological
18 conditions is essential for understanding long-term particulate-matter (PM) variability. Using
19 ground observations from 40 cities, GEOS-FP meteorology, CEDS emissions, and monthly
20 LightGBM models, this study assesses the drivers of PM_{2.5} and PM₁₀ across the Beijing–Tianjin–
21 Hebei (BTH) and Yangtze River Delta (YRD) regions during 2015–2022. The models demonstrate
22 strong predictive skill ($R/R^2 = 0.82/0.67$ for PM_{2.5} and $0.81/0.65$ for PM₁₀), with consistently high
23 performance across cities. Both pollutants exhibit significant decreasing trends over the study period.
24 Counterfactual experiments show that emission reductions overwhelmingly dominate these
25 improvements: PM_{2.5} emission-driven changes intensify from $-9.1 \mu\text{g m}^{-3}$ in 2016 to $-31.4 \mu\text{g m}^{-3}$
26 in 2022, while PM₁₀ reductions strengthen from -9.8 to $-42.9 \mu\text{g m}^{-3}$. Meteorological contributions
27 remain positive (approximately $+2-4 \mu\text{g m}^{-3}$ for PM_{2.5} and $+0.5-3 \mu\text{g m}^{-3}$ for PM₁₀), indicating that
28 air-quality gains were achieved despite meteorological conditions unfavorable to pollutant
29 dispersion. SHAP attribution highlights 2-m air temperature (T2M), humidity (QV2M), and key

precursors (SO₂ total, BC total, NO_x total) as dominant predictors, with interaction patterns showing that meteorological conditions modulate the effectiveness of precursor emissions and associated chemical formation. These results provide a comprehensive, data-driven assessment of the factors shaping PM variability in two major urban clusters of China.

1 Introduction

Particulate matter (PM) is a significant air pollutant and is also a critical research topic in environmental science due to its diverse sources, complex chemical composition, and profound impacts on human health (Zhang et al., 2022a). Classified by aerodynamic diameter, PM_{2.5} (fine particles, $\leq 2.5\mu\text{m}$) and PM₁₀ (inhalable particles, $\leq 10\mu\text{m}$) exert differential impacts on ecosystems and human health owing to their distinct physicochemical properties and environmental behaviors (WHO, 2021). Fine particles (PM_{2.5}) penetrate deep into the lungs and cross the alveolar–blood barrier into systemic circulation, while coarser particles (PM₁₀) deposit predominantly in the upper respiratory tract (Fu et al., 2024). Chronic exposure to PM_{2.5} is linked to respiratory/cardiovascular diseases, declines in lung function, and impairment of the immune system (Franklin et al., 2008; Kioumourtzoglou et al., 2016), Whereas PM₁₀ aggravates asthma , chronic obstructive pulmonary disease (COPD), and other respiratory conditions (Seaton et al., 1995). As two pivotal economic engines of China, the Beijing-Tianjin-Hebei (BTH) and Yangtze River Delta (YRD) regions, characterized by dense industrial clusters and populations, generate substantial industrial and transportation emissions, with high-intensity production and daily activities resulting in long-standing composite air pollution dominated by PM_{2.5}, PM₁₀, and ozone (Dai et al., 2021, 2023), posing persistent threats to human health and urban livability. Furthermore, PM pollution acidifies aquatic environments, disrupts ecosystem balance, degrades soils, and contributes to acid rain and terrestrial biosphere damage (Dominici et al., 2014; Jerrett, 2015).

To address severe air pollution problem, Chinese government implemented the Air Pollution Prevention and Control Action Plan (State Council of the People’s Republic of China, 2013) and the Three-Year Action Plan for Winning the Blue Sky Defense Battle (State Council of the People’s Republic of China, 2018). These initiatives led to substantial reductions in PM concentrations nationwide (Song et al., 2023). However, China's current Ambient Air Quality Standards (GB 3095-

59 2012) stipulate Grade II annual mean limits of $35 \mu\text{g m}^{-3}$ for $\text{PM}_{2.5}$ and $70 \mu\text{g m}^{-3}$ for PM_{10} , which
60 significantly exceed the updated WHO guidelines (AQG 2021).

61 The dynamics of PM are shaped by anthropogenic precursor emissions—sulfur dioxide (SO_2),
62 nitrogen oxides (NO_x), and ammonia (NH_3)—together with meteorological factors such as
63 temperature, humidity, precipitation, pressure, and wind (Xiao et al., 2021). In addition to these
64 inorganic precursors, volatile organic compounds (VOCs) also play an important role in secondary
65 aerosol formation, particularly through pathways leading to secondary organic aerosols, as
66 recognized in numerous atmospheric chemistry studies. $\text{PM}_{2.5}$ originates predominantly from traffic
67 and industrial emissions, combustion processes (e.g., cooking, biomass burning), and secondary
68 formation via atmospheric oxidation to sulfate, nitrate, and organic aerosols (Zhang et al., 2015).
69 PM_{10} also includes coarse particles from fugitive dust (construction, agriculture) and secondary
70 coarse-mode particulates (Wu and Huang, 2021). The SO_2 , NO_x , and NH_3 in the atmosphere can be
71 converted into secondary inorganic aerosols, which significantly regulate PM concentrations (Ding
72 et al., 2019; Feng et al., 2021). Meteorological parameters, such as temperature, relative humidity,
73 precipitation, pressure, and wind, critically influence PM generation, dispersion, and removal
74 (Leung et al., 2018; Zhao et al., 2013). For instance, elevated temperatures accelerate SO_x/NO_x
75 oxidation rates and fine PM formation (Chen et al., 2022). High humidity promotes particle
76 hygroscopic growth, gas-to-particle conversion (e.g., secondary organic aerosols), and wet
77 deposition, thereby altering PM size distribution and lifetime. These PM-meteorology interactions
78 exhibit region- and year-specific nonlinear characteristics (Shen et al., 2017), challenging
79 conventional linear modeling approaches (Zhao et al., 2018)

80 Machine learning (ML), with its capacity to capture complex, nonlinear relationships, has
81 emerged as a powerful tool for atmospheric pollution research (Yin et al., 2022b). ML enhances
82 source apportionment accuracy through multi-source data integration (meteorological, emission,
83 socioeconomic), high-dimensional pattern recognition, and real-time adaptive analysis, enabling
84 identification of complex pollutant interactions (Peng et al., 2024). For $\text{PM}_{2.5}$ and PM_{10} studies, ML
85 facilitates quantitative disentanglement of meteorological and emission contributions, elucidates
86 source-receptor relationships, and informs targeted mitigation strategies.

87 This study employs the LightGBM framework to quantify the drivers of $\text{PM}_{2.5}$ and PM_{10}

88 variability across the BTH and YRD regions during 2015–2022. By leveraging LightGBM’s
89 capability to model nonlinear emission–meteorology–pollution interactions and its efficiency on
90 multi-year, multi-city datasets, the analysis aims to identify the dominant factors governing regional
91 air-quality evolution. The structure of this paper is as follows. Section 2 introduces the datasets used
92 in this study, including national ground-based PM observations (2.1), GEOS-FP meteorological
93 reanalysis fields (2.2), and the CEDS anthropogenic emission inventory (2.3). Section 3 describes
94 the methodological framework. Section 3.1 presents the extraction of city-level meteorological and
95 emission variables from gridded datasets. Section 3.2 outlines the LightGBM modeling workflow,
96 including the feature-engineering strategy (3.2.1), the model training and leave-one-year-out cross-
97 validation procedure (3.2.2), and the SHAP-based interpretation approach (3.2.3). The interannual
98 trend estimation method is detailed in Section 3.3, and the counterfactual framework used to
99 separate meteorological and emission contributions is introduced in Section 3.4. Section 4 reports
100 the main results, including the interannual evolution of PM_{2.5} and PM₁₀ (4.1), machine-learning
101 model performance and key predictor importance (4.2), and the quantified meteorological and
102 emission contributions (4.3). Section 5 provides a broader discussion of the identified driving
103 mechanisms in the context of chemical formation pathways and emission-control policies. Finally,
104 Section 6 summarizes the key findings and presents implications for future air-quality management
105 and research.

106 **2 Data**

107 **2.1 Observational data from national monitoring sites**

108 The ground-level air pollutant data for the YRD and BTH regions were acquired from the
109 China National Environmental Monitoring Center (CNEMC) network (<https://www.cnemc.cn/>, last
110 accessed: December 31, 2022), comprising hourly measurements of PM_{2.5}, PM₁₀, SO₂, NO₂, CO,
111 and O₃ concentrations from 2015 to 2022. Observations from multiple monitoring stations within
112 the same city were averaged to derive city-level pollutant concentrations (site-specific details are
113 provided in Table S1 and Fig. S1). The monitoring network includes 80 stations in the BTH region,
114 covering major cities and areas in Beijing, Tianjin, and Hebei Province, and 197 stations in the YRD
115 region, spanning Shanghai, Jiangsu, Zhejiang, and adjacent provinces. To avoid ambiguity between
116 two cities sharing the same English spelling “Taizhou”, Taizhou City in Jiangsu Province is denoted

117 as TaizhouJS, while Taizhou City in Zhejiang Province is denoted as TaizhouZJ throughout this
118 study.

119 All national monitoring stations strictly follow the Technical Specifications for Automatic
120 Ambient Air Quality Monitoring (Ministry of Environmental Protection of China, 2013a), ensuring
121 standardized field operation and quality control procedures. City-level PM_{2.5} and PM₁₀
122 concentrations are released in accordance with the national reference gravimetric method (Ministry
123 of Environmental Protection of China, 2011), which provides the calibration and traceability
124 framework for automated particulate measurements across the monitoring network. Gaseous
125 pollutants (SO₂, NO₂, CO, and O₃) are measured using ultraviolet fluorescence, chemiluminescence,
126 non-dispersive infrared absorption, and ultraviolet photometric analysis, respectively, following the
127 national specifications for continuous gaseous monitoring (Ministry of Environmental Protection of
128 China, 2013b). These unified procedures ensure accuracy, comparability, and long-term stability of
129 pollutant observations.

130 **2.2 GEOS-FP meteorological data**

131 Meteorological fields for 2015–2022 were obtained from the GEOS Forward Processing
132 (GEOS-FP) product (<http://geoschemdata.wustl.edu/ExtData/>, last accessed: 31 December 2020) at
133 a spatial resolution of 0.25° × 0.3125°. GEOS-FP provides hourly assimilated meteorological
134 variables with relatively high spatial and temporal resolution, enabling refined characterization of
135 mesoscale atmospheric processes over the BTH and YRD regions. Its near–real-time data
136 assimilation framework has been widely applied in regional atmospheric pollution and transport
137 studies, supporting accurate representation of dynamic meteorological conditions (Yin et al., 2021b,
138 2022a, b). Its near–real-time data assimilation system further improves the accuracy of reanalysis-
139 based meteorological fields and enhances representation of dynamic atmospheric processes (Sun et
140 al., 2021a, b; Yin et al., 2019, 2020, 2021a). The meteorological parameters used in this study
141 include total cloud fraction (CLDTOT), precipitation flux (PRECTOT), 2-m specific humidity
142 (QV2M), 2-m air temperature (T2M), sea-level pressure (SLP), surface downward shortwave
143 radiation (SWGDN), and 10-m zonal (U10M) and meridional (V10M) wind components.

144 **2.3 CEDS emission inventory**

145 Anthropogenic emission data for 2015–2022 were obtained from the Community Emissions

146 Data System (CEDs), which provides monthly mean fluxes at a spatial resolution of $0.5^\circ \times 0.5^\circ$. In
147 this study, we use emissions of CH_2O , CO , NH_3 , NO_x , SO_2 , BC , OC , and paraffinic reactive primary
148 emissions (PRPE). Emissions were further categorized into eight sectors: non-combustion
149 agriculture, energy transformation and extraction, industrial combustion and processes, surface
150 transportation, residential and commercial fuel use, solvents, waste treatment and disposal, and
151 international shipping. Anthropogenic emission data for 2015–2022 were derived from the CEDs,
152 a global inventory providing temporally resolved sector-specific emissions. The CEDs framework
153 supports climate change projections and quantifies human-driven interactions between air pollutants
154 and climate systems, critical for assessing health and ecosystem impacts.

155 3 methodology

156 3.1 Emission and meteorological data extraction

157 City-level emission and meteorological variables were derived from gridded emission
158 inventories and meteorological reanalysis datasets.

159 For each city, polygon boundaries were obtained from the GADM Level-2 shapefile, and all grid
160 cells whose centers fell within the city polygon were identified.

161 For emission data, which are expressed as surface fluxes ($\text{kg}\cdot\text{m}^{-2}\cdot\text{s}^{-1}$), the city-scale total
162 emission $E_{\text{city}}(t)$ was obtained by physical integration over all intersecting grid cells:

$$163 \quad E_{\text{city}}(t) = \sum_{i,j} F_{ij}(t) A_{ij} r_{ij} \quad (1)$$

164 where $F_{ij}(t)$ is the emission flux of grid cell (i, j) at time t ; A_{ij} is the nominal grid-cell
165 area; and r_{ij} is the fractional overlap between the grid cell and the city polygon.

166 This area-weighted integration converts surface fluxes into physically consistent city-total
167 emissions.

168 For meteorological variables, which represent intensive state quantities such as near-surface
169 temperature (T2M), specific humidity (QV2M), and wind components (U10M/V10M), city-level
170 averages were computed as the arithmetic mean of all grid-cell centers located inside the city
171 polygon:

$$172 \quad X_{\text{city}}(t) = \frac{1}{N} \sum_{i,j} X_{ij}(t) \quad (2)$$

173 where $X_{ij}(t)$ is the variable value in cell (i, j) , and N is the number of valid grid cells within
174 the city.

175 This center-based averaging is computationally efficient and provides a representative estimate
176 of the mean meteorological condition. Because the study region lies mainly in the mid-to-low
177 latitudes of China, where grid-cell area variation with latitude is minor, this approximation
178 introduces negligible bias compared with full area-weighted averaging.

179 Both extraction procedures ensure spatial consistency between emission and meteorological
180 datasets and yield temporally continuous, city-level time series for subsequent modeling.

181 **3.2 LightGBM modeling**

182 Light Gradient Boosting Machine (LightGBM) is an efficient and scalable implementation of
183 gradient boosting, extensively applied to regression, classification, and ranking tasks (Yin et al.,
184 2021c). By using a histogram-based decision-tree algorithm, the LightGBM model drastically
185 reduces both computation time and memory usage compared to traditional gradient-boosting
186 methods such as XGBoost (Bian et al., 2023; Zhang et al., 2017). It supports the direct handling of
187 categorical variables without one-hot encoding, improving efficiency when processing high-
188 dimensional datasets. During training, LightGBM grows trees in a leaf-wise (best-first) manner,
189 generating deeper splits along the branch that achieves the largest loss reduction.

190 In contrast, XGBoost and classical Gradient Boosting Decision Trees (GBDT) use a level-wise
191 growth strategy, which provides stability but can become computationally slower for large-scale
192 data. LightGBM also offers extensive hyperparameter controls, such as maximum tree depth,
193 minimum data in leaf, and feature fraction, to balance model complexity and generalization (Ke et
194 al., 2017). Due to its high predictive accuracy, efficient splitting mechanism, and robust
195 computational capability, LightGBM has become one of the most widely used gradient-boosting
196 frameworks in environmental modeling (Liu et al., 2023; Wang et al., 2022; Zhang et al., 2022b).

197 Prior to model training, all hourly emission and meteorological inputs were aggregated to
198 monthly means, and the LightGBM models were trained on these monthly-resolved datasets. This
199 temporal aggregation ensured that all variables shared the same temporal frequency, preventing
200 inconsistencies between hourly and monthly features. It also matched the model input scale with
201 the monthly trend analysis period (2015–2022), thereby avoiding time-scale mismatches between
202 predictor variables and the evaluation framework.

203 The model performance was evaluated using three widely recognized regression metrics: the
204 correlation coefficient (R), indicating the linear relationship between predicted and observed
205 concentrations. the coefficient of determination (R^2), measuring the proportion of variance in
206 observations explained by the model; and the root-mean-square error (RMSE), representing the
207 average magnitude of prediction errors. Higher R and R^2 and lower RMSE indicate stronger
208 predictive ability.

209 **3.2.1 Feature Engineering**

210 To ensure interpretability and reduce redundancy, all anthropogenic emissions were aggregated
 211 into a single total value for each species (e.g., NOx_total, SO2_total). Rather than treating sector-
 212 resolved emissions separately, emissions from all sectors were summed into one unified variable
 213 per pollutant. This consolidation reduces feature dimensionality, mitigates multicollinearity among
 214 sectoral components, and preserves the dominant emission signal, resulting in a more compact and
 215 interpretable model structure.

216 To incorporate temporal information, three seasonal descriptors were introduced: (1) a pair of
 217 harmonic terms (month_sin and month_cos) representing the cyclic annual progression; (2) a
 218 categorical season indicator to reflect broad seasonal regimes. These features provide smooth,
 219 physically meaningful representations of seasonality without imposing sharp discontinuities
 220 between months.

221 In addition, two derived emission indicators were constructed to characterize temporal
 222 variability and multi-scale coupling:

223 Seasonal difference (sdiff) represents interannual seasonal changes over a 12-month interval.
 224 For each feature x , the seasonal difference is defined as:

$$225 \text{sdiff}_t(x) = \frac{x_t - x_{t-1}}{2} \quad (3)$$

226 where x_t denotes the monthly mean value at time t . This feature highlights annual-scale variations
 227 and helps the model capture year-to-year emission variability under identical seasonal conditions.

228 Rolling detrended residual (detr) represents short-term deviations from a 12-month moving-
 229 mean trend. It is expressed as:

$$230 \text{detr}_t(x) = x_t - \mu_t^{(12)}(x) \quad (4)$$

$$231 \mu_t^{(12)}(x) = \frac{1}{k_t} \sum_{i=t-11}^t x_i \cdot \mathbf{1}_{\{x_i \text{ valid}\}}, \quad k_t \geq 3 \quad (5)$$

232 Where $\mu_t^{(12)}(x)$ is the rolling mean computed over the past 12 months, requiring at least three
 233 valid data points ($k_t \geq 3$). This feature isolates short-term fluctuations by removing low-frequency
 234 seasonal trends.

235 In practice, the final predictor set comprised 35 variables: eight monthly meteorological
 236 parameters, eight species-level aggregated emission totals (e.g., NOx_total, SO2_total, BC_total),
 237 three temporal descriptors (month_sin, month_cos, season), and two derived indicators (sdiff and

238 detr) for each emission species. Pollutant concentrations and explicit calendar identifiers (year,
239 month, date) were excluded from the input space to avoid information leakage and to ensure
240 consistent temporal treatment. A complete list of variables used in the model is provided in Table
241 S2.

242 **3.2.2 Model Training and Cross-Validation Procedure**

243 Before model fitting, all months with missing PM_{2.5} or PM₁₀ observations were removed to
244 ensure consistency between predictors and targets. The derived emission features (sdiff and detr)
245 inherently contain missing values during their initial 12-month computation window; these were
246 addressed using a simple mean-imputation strategy applied within each training fold. Specifically,
247 missing entries for each feature were replaced with the corresponding feature mean computed solely
248 from the training subset of that fold, thereby preventing temporal leakage and ensuring that
249 imputation relied exclusively on information available before prediction.

250 The LightGBM model was independently trained for each city, pollutant type (PM_{2.5} and PM₁₀),
251 and cross-validation fold. A leave-one-year-out (LOGO) cross-validation scheme was adopted,
252 whereby data from a single year were held out for testing while the remaining seven years were
253 used for training. This process was repeated sequentially so that each year between 2015 and 2022
254 served once as the held-out test period. The resulting predictions thus constitute out-of-sample
255 estimates for every year, providing a conservative and temporally robust assessment of model
256 generalizability and avoiding within-year information leakage.

257 Within each training subset, a randomized search procedure was used to identify the optimal
258 hyperparameter configuration. Ten candidate parameter sets were sampled from predefined
259 distributions and evaluated using three-fold internal cross-validation, with the negative mean
260 squared error (MSE) serving as the scoring metric. The optimized parameters included learning_rate,
261 n_estimators, num_leaves, max_depth, min_child_samples, subsample, colsample_bytree,
262 reg_alpha, and reg_lambda, all drawn from physically plausible ranges. Other settings, such as
263 objective = regression, metric = rmse, early_stopping_rounds = 20, and random_state = 42, were
264 held constant across folds to ensure comparability. A consolidated summary of the optimized
265 hyperparameter ranges is presented in Table S3.

266 **3.2.3 SHAP Interpretation Analysis**

267 To interpret the LightGBM outputs and quantify the contribution of individual predictors, the
 268 Shapley Additive explanations (SHAP) framework was applied. For each trained model, SHAP
 269 values $s_{i,j}$ represent the marginal contribution of feature j to the prediction of sample i . They are
 270 derived from cooperative game theory and satisfy the local additivity principle:

$$271 \quad f(x_i) = E[f(x)] + \sum_{j=1}^m s_{i,j} \quad (6)$$

272 where $f(x_i)$ is the model prediction for sample i , and $E[f(x)]$ is the expected model
 273 output over all samples.

274 Because this study involves multiple cities across the BTH and YRD regions, a unified regional
 275 SHAP ranking was derived by weighting each SHAP importance of city by its corresponding
 276 number of valid monthly samples. The weighted importance for feature j is defined as:

$$277 \quad I_j^{(w)} = \frac{\sum_{c=1}^N I_{j,c} n_c}{\sum_{c=1}^N n_c} \quad (7)$$

278 Here $I_{j,c}$ is the SHAP-based importance of feature j in city c , and n_c is the number of
 279 valid samples for that city, N is the total number of cities.

280 This weighting strategy ensures that cities with longer and more complete observational
 281 records have proportionally greater influence on the regional-level interpretability.

282 **3.3 Interannual trend analysis method**

283 To quantify the interannual trends of PM_{2.5} and PM₁₀ concentrations from 2015 to 2022, a linear
 284 regression model was employed in this study. For each city, the relationship between annual mean
 285 concentration y and year x was modeled as:

$$286 \quad y = \beta_0 + \beta_1 x + \epsilon \quad (8)$$

287 where β_0 represents the intercept (baseline concentration), and ϵ denotes the error term. The
 288 slope β_1 , reflecting the annual rate of concentration change, was estimated via the ordinary least
 289 squares (OLS) method. Specifically, the parameters were optimized by minimizing the residual sum
 290 of squares (RSS):

$$291 \quad \arg \min_{\beta_0, \beta_1} \sum_{i=1}^n (y_i - (\beta_0 + \beta_1 x_i))^2 \quad (9)$$

292 where n is the sample size (e.g., $n=6$ for the period 2015–2022), x_i denotes the year, and y_i
 293 represents the corresponding annual mean concentration.

294 The slope β_1 was derived as:

$$295 \quad \beta_1 = \frac{\text{Cov}(x, y)}{\text{Var}(x)} \quad (10)$$

296 The sign of β_1 indicates the direction of concentration trends (negative for decreasing,
297 positive for increasing), while its absolute value quantifies the magnitude of change.

298 **3.4 Methodology for disentangling meteorological and emission contributions**

299 To quantify meteorological and anthropogenic emission contributions, the trained models were
300 applied in a parallel prediction experiment. For each year from 2016 to 2022, anthropogenic
301 emission features were held fixed at their 2015 levels, while meteorological and temporal predictors
302 were retained at their actual contemporaneous values. This produced a counterfactual concentration
303 series driven solely by meteorological variability. This yielded pollutant concentrations driven
304 solely by meteorological variations (denoted as $ML_{2022\text{met}}$ for 2022). The contribution metrics
305 related to 2015 were calculated as follows:

306 Meteorological contribution ($ML_{2022\text{met}}$):

$$307 \quad ML_{2022\text{met}} = ML_{15-22} - ML_{2015} \quad (11)$$

308 ML_{15-22} is the non-emission condition unchanged, the emission condition is fixed as the model
309 prediction result in 2015, and ML_{2015} is the model prediction result with unchanged meteorological
310 and emission conditions.

311 Emission contribution ($ML_{2022\text{emis}}$):

$$312 \quad ML_{2022\text{emis}} = (Obs_{2022} - Obs_{2015}) - ML_{2022\text{met}} \quad (12)$$

313 Obs_{2022} and Obs_{2015} : Observed concentrations in 2022 and 2015, respectively.

314 **4 Results**

315 **4.1 Interannual trends of ground-level PM_{2.5} and PM₁₀**

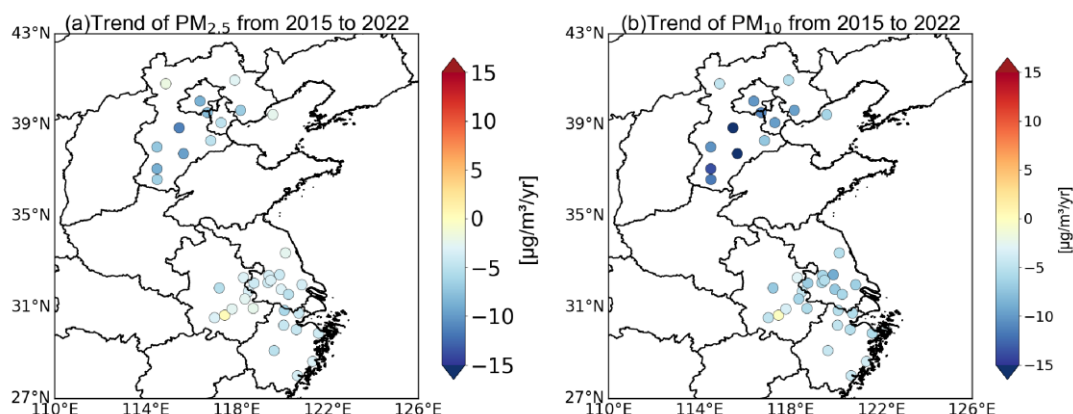
316 Fig. 1 illustrates the interannual evolution of ground-level PM_{2.5} and PM₁₀ concentrations
317 across the BTH and YRD regions from 2015 to 2022, with corresponding annual mean spatial
318 distributions shown in Fig. S2–S3. Both pollutants exhibit persistent downward trajectories across
319 nearly all cities. The monthly time series and associated OLS trend lines (Fig. S4) further confirm
320 that these declines remain stable throughout the study period, with the most pronounced reductions
321 occurring before 2020. Statistical diagnostics from linear regression (Table S4) indicate that most
322 cities display significant negative trends ($p < 0.05$), underscoring the robustness and consistency of

323 these decreases.

324 For PM_{2.5}, all cities show negative trends, with annual rates ranging from approximately -1.53
325 to -9.46 $\mu\text{g m}^{-3} \text{ yr}^{-1}$. Within BTH, the most rapid declines occur in Baoding ($-9.46 \pm 0.74 \mu\text{g m}^{-3}$
326 yr^{-1}), Hengshui ($-8.36 \pm 0.67 \mu\text{g m}^{-3} \text{ yr}^{-1}$), and Xingtai ($-8.02 \pm 0.56 \mu\text{g m}^{-3} \text{ yr}^{-1}$), while Chengde
327 ($-1.98 \pm 0.35 \mu\text{g m}^{-3} \text{ yr}^{-1}$) and Zhangjiakou ($-2.00 \pm 0.42 \mu\text{g m}^{-3} \text{ yr}^{-1}$) exhibit more modest declines.
328 In the YRD region, substantial decreases are observed in Huzhou ($-5.69 \pm 1.22 \mu\text{g m}^{-3} \text{ yr}^{-1}$), Hefei
329 ($-4.83 \pm 0.33 \mu\text{g m}^{-3} \text{ yr}^{-1}$), and Chuzhou ($-4.28 \pm 1.12 \mu\text{g m}^{-3} \text{ yr}^{-1}$), whereas Zhoushan ($-2.11 \pm$
330 $0.14 \mu\text{g m}^{-3} \text{ yr}^{-1}$) and Taizhou-ZJ ($-2.72 \pm 0.26 \mu\text{g m}^{-3} \text{ yr}^{-1}$) experience comparatively smaller
331 reductions. These regional contrasts closely align with the initial concentration levels shown in Fig.
332 S2, where inland BTH cities began with substantially higher baselines (e.g., Baoding and Hengshui
333 exceeded 105 and 98 $\mu\text{g m}^{-3}$ in 2015), enabling larger absolute declines.

334 For PM₁₀, all cities also exhibit significant decreases, with annual trends ranging from roughly
335 -1.84 to -13.79 $\mu\text{g m}^{-3} \text{ yr}^{-1}$. The largest reductions occur in BTH, particularly Hengshui ($-13.79 \pm$
336 $1.82 \mu\text{g m}^{-3} \text{ yr}^{-1}$), Baoding ($-13.07 \pm 1.46 \mu\text{g m}^{-3} \text{ yr}^{-1}$), and Xingtai ($-12.76 \pm 1.29 \mu\text{g m}^{-3} \text{ yr}^{-1}$). In
337 contrast, Chizhou ($-1.84 \pm 2.03 \mu\text{g m}^{-3} \text{ yr}^{-1}$) and Zhoushan ($-2.77 \pm 0.30 \mu\text{g m}^{-3} \text{ yr}^{-1}$) show the
338 smallest declines, and the PM₁₀ trend in Chizhou is not statistically significant ($p = 0.40$), consistent
339 with its minimal decline rate. As with PM_{2.5}, cities starting with the highest PM₁₀ levels—such as
340 Baoding (174.6 $\mu\text{g m}^{-3}$ in 2015) and Hengshui (175.9 $\mu\text{g m}^{-3}$)—exhibit the steepest reductions,
341 whereas cities with lower initial levels (e.g., Zhoushan at $\sim 46.8 \mu\text{g m}^{-3}$) show correspondingly
342 smaller absolute decreases.

343 Overall, both PM_{2.5} and PM₁₀ decrease more rapidly in BTH than in YRD, reflecting regional
344 differences in initial emissions, industrial structure, and the intensity of mitigation policies. The
345 widespread statistical significance of the trends (Table S4) supports the conclusion that both regions
346 experienced sustained and robust improvements in air quality during 2015–2022.



347

348 **Fig. 1** Interannual variation trends of PM_{2.5} (a) and PM₁₀ (b) in each city during 2015-2022.

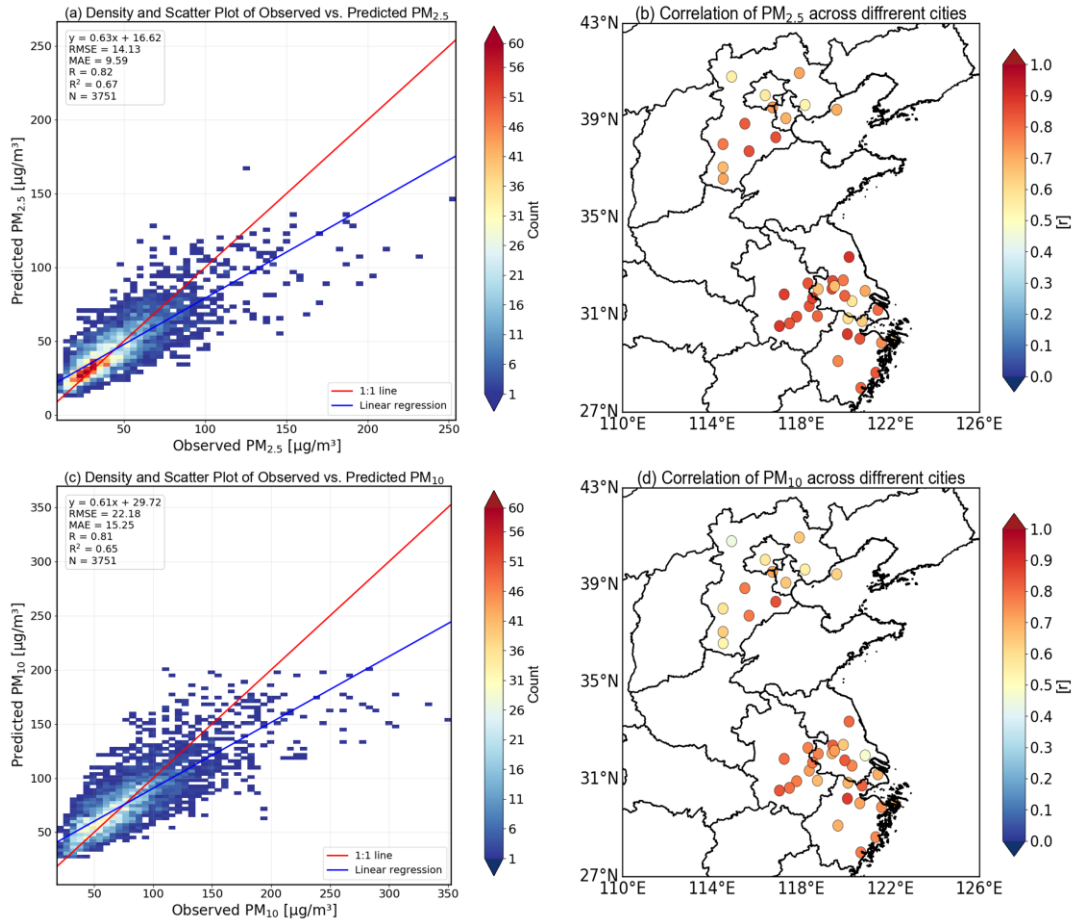
349 **4.2 Machine learning model performance and variable importance**

350 Fig. 2 shows the predictive performance of the LightGBM models for PM_{2.5} and PM₁₀ across
 351 all cities. The density scatterplots (Fig. 2a and 2c) indicate strong agreement between predictions
 352 and observations, with $R/R^2 = 0.82/0.67$ for PM_{2.5} and $0.81/0.65$ for PM₁₀. Consistent performance
 353 is also observed at the city level (Fig. 2b and 2d), and the full statistics provided in Table S5
 354 demonstrate that most cities achieve $R > 0.70$, confirming the robustness of the models across
 355 diverse urban settings.

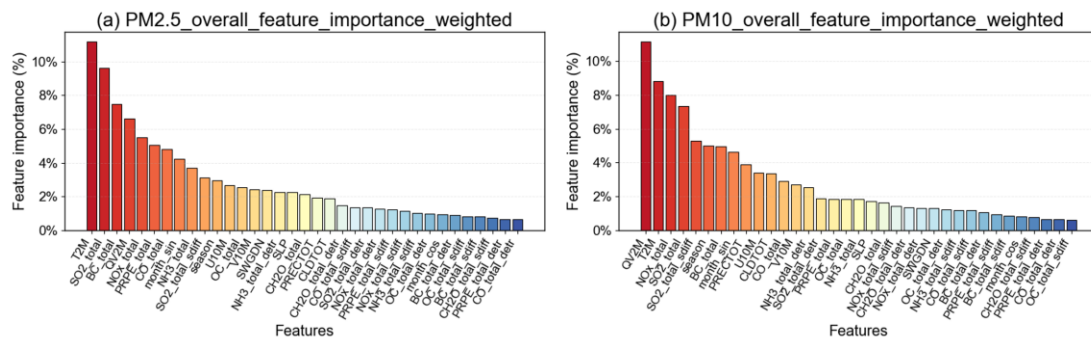
356 Fig. 3 summarizes the SHAP-based overall feature importance. For PM_{2.5}, although T2M ranks
 357 as the single most influential variable in Fig. 3a, the broader pattern shows that emission-related
 358 predictors dominate the upper portion of the importance distribution, with SO₂_total, BC_total, and
 359 NOx_total collectively contributing a larger share than any single meteorological factor. This
 360 implies that PM_{2.5} variability during 2015–2022 remains strongly controlled by precursor emissions
 361 and their long-term reductions. In contrast, for PM₁₀ (Fig. 3b), meteorological variables, especially
 362 QV2M and T2M, occupy the highest ranks, reflecting the greater role of humidity and temperature
 363 in modulating coarse particles through hygroscopic growth, boundary-layer dynamics, and seasonal
 364 resuspension processes. While NOx_total and SO₂_total remain important, their relative influence
 365 is smaller than in PM_{2.5}, consistent with PM₁₀'s stronger coupling to meteorology.

366 Region-specific SHAP rankings (Fig. S5) further show that PM_{2.5} in BTH is more strongly
 367 influenced by SO₂_total and BC_total, whereas YRD exhibits a greater sensitivity to meteorological
 368 factors such as temperature and humidity. For PM₁₀, QV2M is the dominant driver in both regions,

369 but precursor importance (e.g., NO_x_total) remains higher in BTH. These spatial contrasts highlight
 370 differing emission structures and seasonal behaviors between regions, underscoring the need for
 371 differentiated control strategies for PM_{2.5} and PM₁₀.



372
 373 **Fig. 2** The density scatter plots of PM_{2.5} (a) and PM₁₀ (c) concentrations observed and predicted,
 374 respectively. The correlation of PM_{2.5} (b) and PM₁₀ (d) in each city over BTH and YRD regions,
 375 respectively.



376
 377 **Fig. 3** The feature importance of rankings of PM_{2.5} (a) and PM₁₀ (b) in ML model prediction,
 378 respectively.

379 **4.3 Contributions of emissions and meteorology**

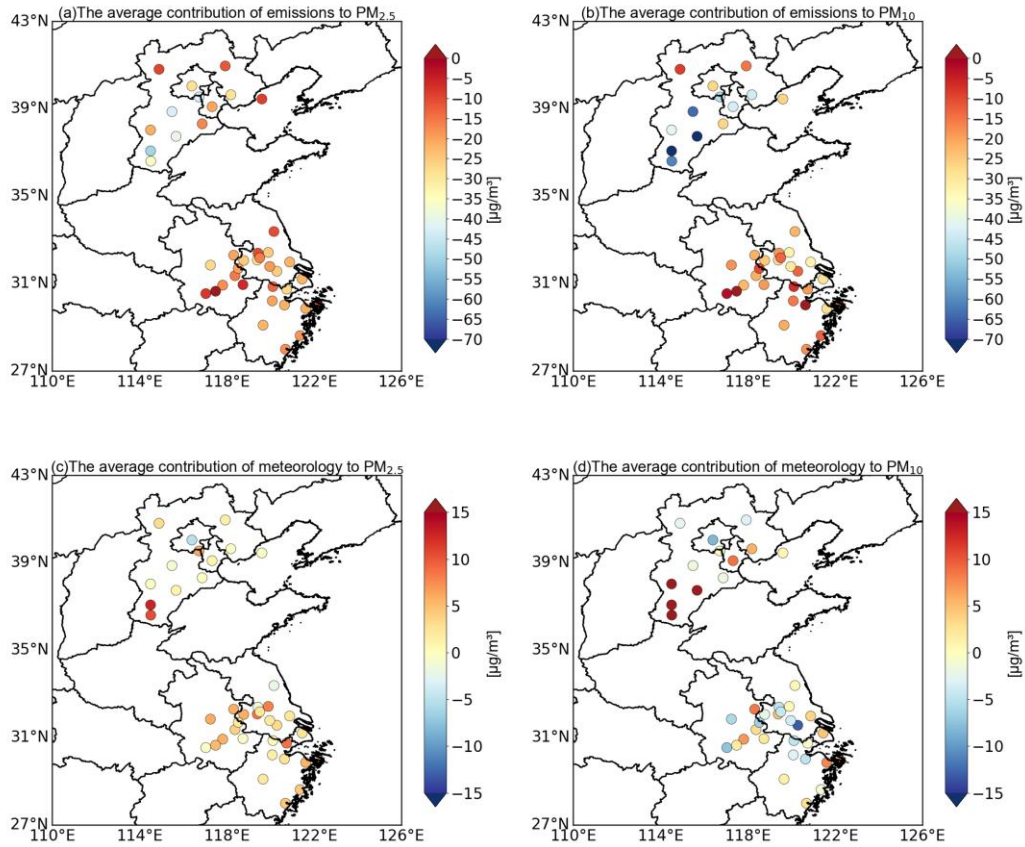
380 The spatial patterns of average emission and meteorological contributions (Fig. 4) reveal clear
381 regional contrasts between northern cities in BTH and southern cities in YRD. For $PM_{2.5}$, emission
382 contributions are strongly negative across most BTH cities such as Baoding, Hengshui, and Xingtai,
383 often exceeding $-30 \mu\text{g m}^{-3}$, reflecting substantial reductions from historically elevated emission
384 levels. In contrast, YRD cities such as Suzhou, Hangzhou, and Ningbo display more moderate
385 negative contributions, typically around -10 to $-20 \mu\text{g m}^{-3}$, consistent with their lower baseline
386 emissions. Meteorological contributions also exhibit north–south gradients: several coastal or
387 humid subtropical YRD cities (e.g., Ningbo, Wenzhou) show slightly positive meteorological
388 influences, whereas continental BTH cities (e.g., Beijing, Tianjin) show predominantly negative
389 effects associated with winter stagnation, shallow boundary layers, and lower humidity. Similar
390 spatial patterns are observed for PM_{10} (Fig. 4b, d), where emission-driven reductions remain larger
391 in BTH than in YRD, mirroring regional differences in emission intensity.

392 The interannual evolution shown in Fig. 5 further clarifies these relationships. Emission
393 contributions remain consistently negative from 2016 to 2022 for both pollutants and intensify over
394 time. For $PM_{2.5}$, the reductions increase from $-9.13 \mu\text{g m}^{-3}$ in 2016 to $-31.39 \mu\text{g m}^{-3}$ in 2022, while
395 PM_{10} reductions strengthen from -9.77 to $-42.91 \mu\text{g m}^{-3}$ over the same period. These progressively
396 stronger negative contributions align with downward trends in major emission species, including
397 NO_x _total, SO_2 _total, and BC_total. In contrast, meteorological contributions remain positive
398 throughout all years, approximately 2 – $4 \mu\text{g m}^{-3}$ for $PM_{2.5}$ and 0.5 – $3 \mu\text{g m}^{-3}$ for PM_{10} , indicating that
399 annual meteorological conditions generally acted to increase particulate levels rather than suppress
400 them. Although PM_{10} is often considered more responsive to meteorological variability, its smaller
401 meteorological contributions here largely reflect the substantially faster decline in PM_{10} emissions
402 during 2016–2022, which leaves less residual variability to be attributed to meteorology. In addition,
403 $PM_{2.5}$ formation is strongly modulated by temperature- and humidity-dependent secondary
404 processes, such as nitrate formation and hygroscopic growth, whereas PM_{10} is dominated by
405 mechanically generated particles that respond more weakly to these meteorological drivers.

406 Temporal relationships between individual emission indicators and their contributions are
407 shown in Fig. 6 For $PM_{2.5}$, monthly variations in NO_x _total, SO_2 _total, and BC_total exhibit strong
408 correlations with their respective emission contributions ($R = 0.89$ – 0.95). Similar correspondence

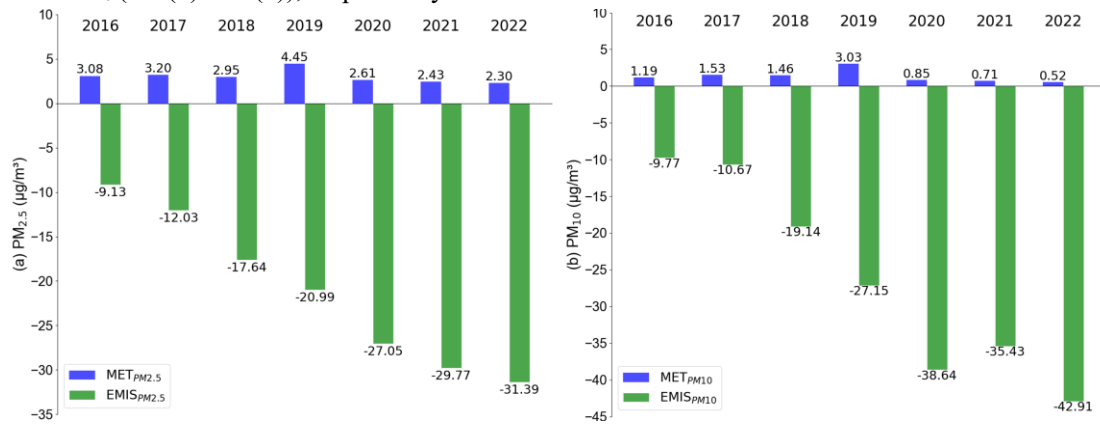
409 is found for PM₁₀ (R = 0.89–0.93). These high correlations indicate that the estimated emission
410 contributions track the month-to-month emission variability in a physically consistent way: months
411 with higher emissions correspond to greater positive contributions to particle levels, whereas months
412 with lower emissions correspond to diminished contributions. This coherence holds despite
413 nonlinear model responses, which adjust contribution magnitudes according to the concurrent
414 meteorological and chemical environment. Meteorological drivers display opposite temporal
415 behavior (Fig. 7). Temperature and humidity show strong negative correlations with their
416 meteorological contributions for both pollutants (R ≈ −0.96 to −0.98), indicating that lower
417 temperatures or reduced moisture tend to increase particulate levels, while warmer or wetter periods
418 are associated with weaker contributions. This behavior is consistent with well-understood seasonal
419 differences in atmospheric mixing and humidity-driven processes.

420 Taken together, the dominance of increasingly negative emission contributions (Fig. 5),
421 combined with the generally positive meteorological contributions, indicates that improvements in
422 PM_{2.5} and PM₁₀ were achieved despite meteorological conditions that tended to enhance particle
423 levels. Emissions therefore play the central role in explaining the observed multi-year declines
424 across both pollutants.



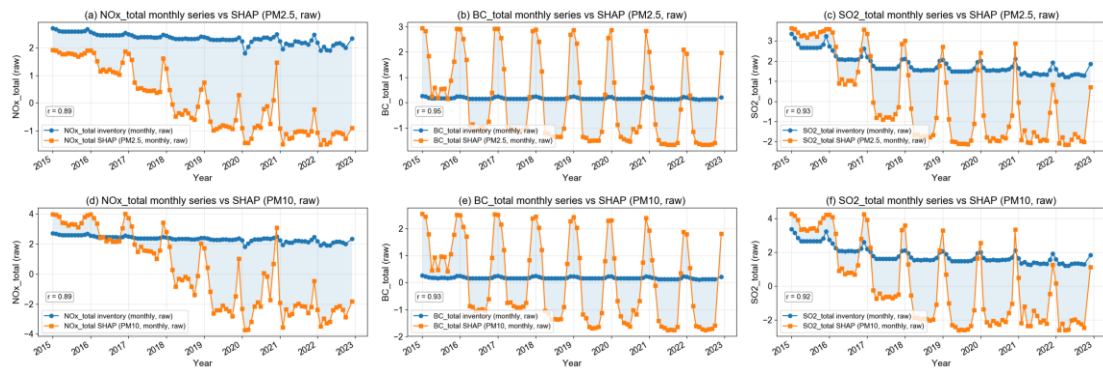
425
426
427

Fig. 4 The average contributions of emissions and meteorological variables to $PM_{2.5}$ (for (a) and (c)) and PM_{10} (for (b) and (d)), respectively.

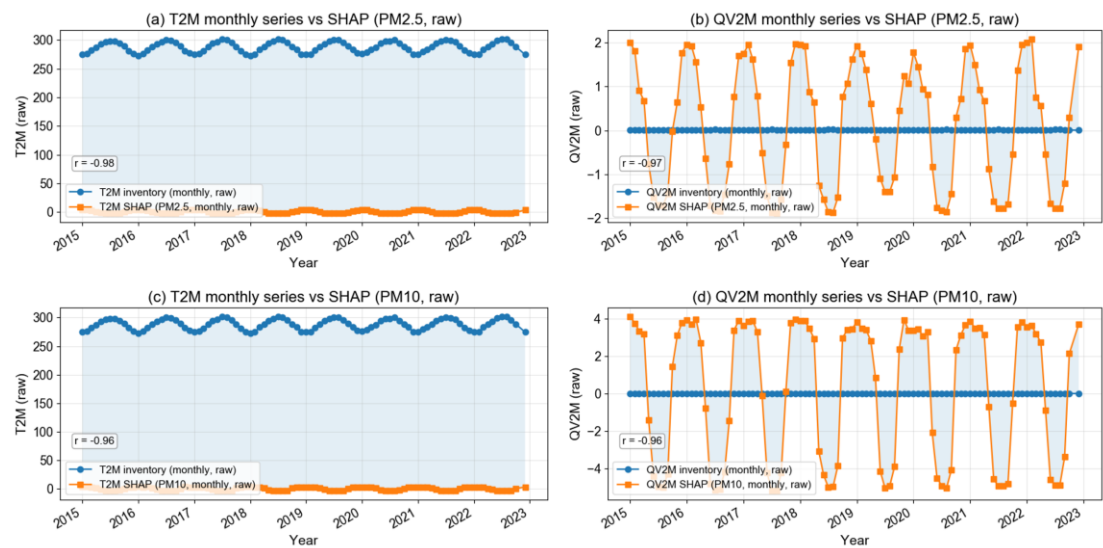


428
429
430

Fig. 5 The averaging the emission or meteorological contributions to $PM_{2.5}$ (a) and PM_{10} (b) of each year relative to 2015.



431
 432 **Fig. 6** Monthly emission inventories of NO_x_total, BC_total, and SO₂_total and their corresponding
 433 SHAP values for PM_{2.5} and PM₁₀ from 2015 to 2022. Panels (a)–(c) show NO_x_total, BC_total,
 434 and SO₂_total versus SHAP contributions for PM_{2.5}, while panels (d)–(f) present the corresponding
 435 relationships for PM₁₀.



436
 437 **Fig. 7** Monthly meteorological variables (T2M and QV2M) and their corresponding SHAP values
 438 for PM_{2.5} and PM₁₀ from 2015 to 2022. Panels (a)–(b) show the relationships for PM_{2.5}, and panels
 439 (c)–(d) show the corresponding results for PM₁₀.

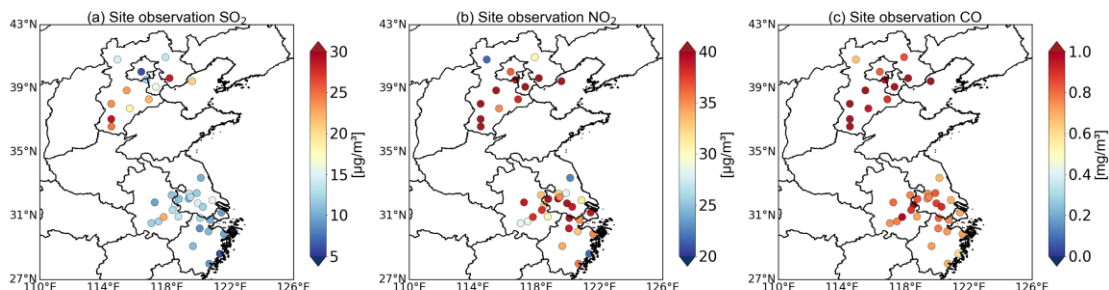
440 **5 Discussions**

441 To support the physical interpretation of the SHAP-derived attributions, we first examine the
 442 spatial distributions and statistical relationships of key precursors. Fig. 8 shows that the ambient
 443 concentrations of CO, NO₂, and SO₂ exhibit pronounced spatial contrasts across the BTH and YRD
 444 regions. Heavy industrial cities such as Tangshan, Xingtai, Handan, and Baoding maintain the
 445 highest levels of all three pollutants, whereas coastal YRD cities such as Zhoushan and TaizhouZJ
 446 display substantially lower concentrations due to cleaner energy structures and reduced coal-
 447 intensive activities. These spatial patterns provide important context for the correlation results
 448 summarized in Table 1 CO exhibits the strongest association with PM_{2.5} (mean R ≈ 0.72) and

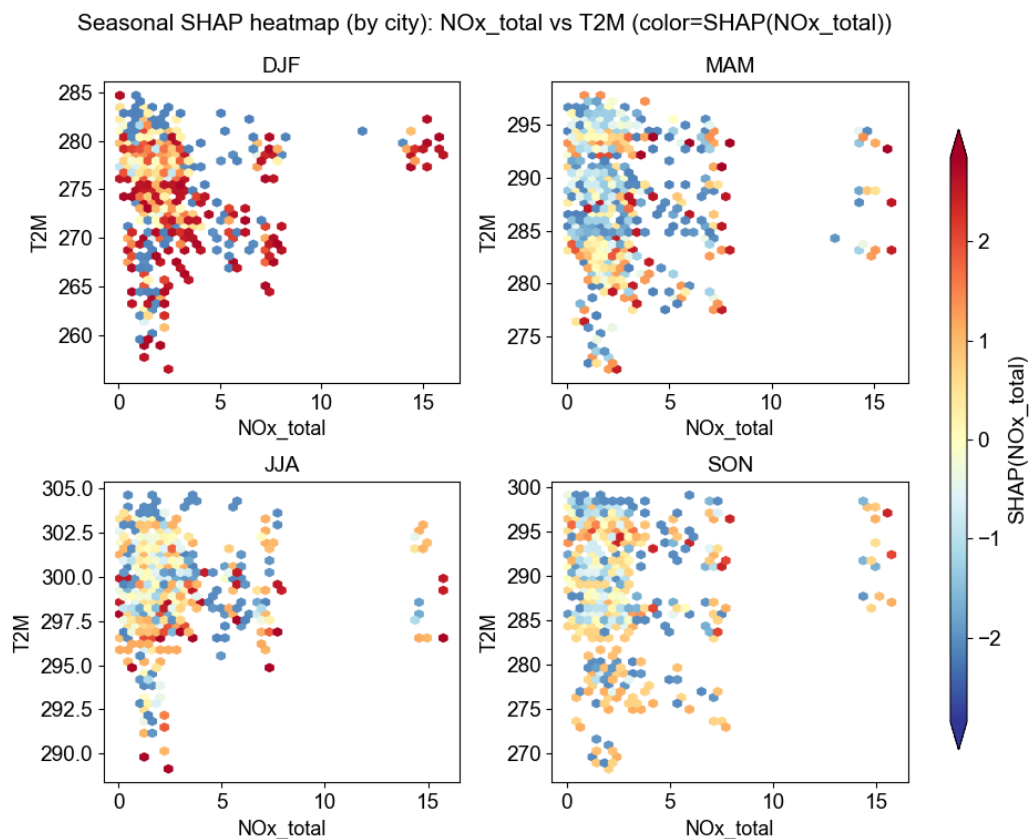
449 PM₁₀ (mean R ≈ 0.62), followed by NO₂ (R ≈ 0.59/0.57) and SO₂ (R ≈ 0.49/0.48). The
450 dominance of PM_{2.5}–CO covariation reflects their shared combustion origins, including vehicle
451 exhaust, industrial boilers, and winter heating, and aligns with recent multi-platform and top-down
452 studies showing that CO, NO_x, carbonaceous aerosols, and combustion-related PM_{2.5} arise from
453 tightly coupled fuel-burning processes and jointly contribute to CO₂ and black carbon
454 budgets(Tiwari et al., 2025; Wang et al., 2021, 2025). In contrast, consistently weaker SO₂
455 correlations, despite elevated SO₂ levels in several northern cities, reflect the substantial
456 effectiveness of nationwide desulfurization policies, which have suppressed sulfate formation while
457 shifting secondary aerosol chemistry toward nitrate-dominated regimes. NO₂ correlations fall
458 between those of CO and SO₂, indicating persistent contributions from traffic and industrial sources
459 but increasing modulation by evolving chemical pathways and long-term emission controls. These
460 correlation structures also contextualize the temperature, NO_x total interaction patterns. Across the
461 observational range, lower temperatures correspond to markedly stronger NO_x-related contributions
462 to PM_{2.5}, consistent with enhanced ammonium nitrate stability and reduced boundary-layer mixing
463 during cold-season stagnation. At higher temperatures, the influence of NO_x total progressively
464 weakens due to thermodynamic limitations on nitrate formation and increased vertical dilution. This
465 interaction pattern, illustrated in Fig. 9, extends naturally from the emission–PM_{2.5} relationships
466 revealed in Fig. 8 and Table 1, showing that NO_x total remains an influential precursor but its
467 chemical effectiveness is strongly conditioned by temperature. A comparable interaction is not
468 examined for PM₁₀, as coarse particles are more strongly shaped by mechanical dust, resuspension,
469 and surface-driven processes, leading to less consistent temperature-dependent chemical behavior.
470 Likewise, we do not present a QV2M–precursor interaction panel: humidity influences multiple
471 competing processes such as hygroscopic growth, aqueous-phase reactions, boundary-layer
472 suppression, and wet removal. These intertwined effects obscure a singular mechanistic relationship
473 with SO₂ at the seasonal scale, making the interaction less suitable for clear physical interpretation.

474 Taken together, these results outline a coherent emission–chemical transformation–
475 meteorological coupling framework: combustion-related pollutants such as CO, NO₂, and SO₂ co-
476 vary with PM_{2.5} because they originate from shared fuel-burning sources; evolving chemical
477 pathways, most notably the post-desulfurization transition toward nitrate-dominated secondary

478 formation, modulate the strength of these associations; and meteorological conditions, particularly
 479 temperature, further amplify or suppress the efficiency of secondary inorganic aerosol production.
 480 This integrated perspective underscores the need for PM_{2.5} mitigation strategies that jointly consider
 481 precursor reductions, seasonal chemical regimes, and meteorological variability.



482
 483 **Fig. 8** The average concentrations of SO₂ (a), NO₂ (b), CO (c), respectively, during 2015 to 2020
 484 over BTH and YRD regions.



485
 486 **Fig. 9** Seasonal scatter plots of NO_x_total versus T2M across all cities, with point colors representing
 487 the SHAP contribution of NO_x_total. The four panels correspond to the DJF, MAM, JJA, and SON
 488 seasons.

489 **Table 1** The correlation values among SO₂, NO₂, CO and PM_{2.5} / PM₁₀, respectively.

| | SO ₂ | NO ₂ | CO |
|--|-----------------|-----------------|----|
|--|-----------------|-----------------|----|

| | | | |
|-------------------|------|------|------|
| PM _{2.5} | 0.49 | 0.59 | 0.72 |
| PM ₁₀ | 0.48 | 0.57 | 0.62 |

490 **6 Conclusions**

491 This study integrates multi-source emission inventories, GEOS-FP meteorological fields, and
492 ground-based observations to investigate the drivers of PM_{2.5} and PM₁₀ variability across the BTH
493 and YRD regions over 2015–2022 using a unified LightGBM modeling and attribution framework.
494 Both pollutants exhibit clear and statistically significant declines across most cities, supported by
495 strong model performance under a rigorous leave-one-year-out cross-validation design (R/R² =
496 0.82/0.67 for PM_{2.5}; 0.81/0.65 for PM₁₀). The consistent agreement between predictions and
497 observations across regions and years demonstrates the robustness of the machine learning
498 representation of emission–meteorology–PM interactions.

499 A key contribution of this work lies in the incorporation of SHAP-based interpretability
500 diagnostics, which allow the model to remain physically traceable while leveraging nonlinear
501 learning capabilities. The attribution experiments clearly indicate that anthropogenic emission
502 reductions are the dominant driver of PM improvements. For PM_{2.5}, emission-driven decreases
503 intensify from $-9.13 \mu\text{g m}^{-3}$ in 2016 to $-31.39 \mu\text{g m}^{-3}$ in 2022; for PM₁₀, corresponding reductions
504 strengthen from -9.77 to $-42.91 \mu\text{g m}^{-3}$. These progressively stronger negative contributions are
505 consistent with sustained declines in NO_x, SO₂, and BC emissions. In contrast, meteorological
506 contributions remain positive in all years, indicating that prevailing weather conditions generally
507 acted to increase particle levels rather than suppress them. The monthly coherence between
508 precursor emissions and their SHAP-derived contributions, together with physically interpretable
509 temperature and humidity meteorological patterns, provides additional internal validation of the
510 model’s mechanistic consistency.

511 These results highlight several strengths of the proposed framework. The use of harmonized
512 monthly emission totals, multi-scale temporal descriptors (sdiff and detr), and SHAP interaction
513 assessment enables a physically grounded interpretation of complex emission–meteorology
514 coupling. The explicit construction of counterfactual predictions offers a transparent means of
515 separating meteorological and anthropogenic influences. Collectively, these methodological
516 elements provide a reproducible pathway for extending machine-learning-based attribution studies

517 [to other regions or pollutants.](#)

518 Despite these advantages, several limitations remain. The monthly temporal resolution cannot
519 fully resolve short-term meteorological or chemical processes; uncertainties in bottom-up emission
520 inventories and meteorological reanalyses may influence the absolute magnitudes of estimated
521 contributions; and, as with all empirical models, causality cannot be inferred directly from statistical
522 relationships. Future work may integrate higher-frequency observations, additional chemical
523 precursors (e.g., VOCs), or hybrid machine-learning–chemical transport approaches to further
524 improve process interpretability and mechanistic fidelity.

525 Overall, this study demonstrates that multi-sector anthropogenic emission reductions rather
526 than meteorological variability primarily explain the observed decreases in PM_{2.5} and PM₁₀ from
527 2015 to 2022, and that physically informed machine-learning tools, coupled with SHAP
528 interpretability, provide a powerful framework for diagnosing multi-pollutant air-quality evolution
529 and supporting evidence-based emission control strategies.

530

531 **Code and data availability**

532 [The code and data for this study can be found on https://doi.org/10.5281/zenodo.17779780.](https://doi.org/10.5281/zenodo.17779780)

533

534 **Competing interests**

535 The contact author has declared that none of the authors has any competing interests.

536

537 **Acknowledgements**

538 This work is jointly supported by Excellent Young Scientists Fund of the National Natural Science
539 Foundation of China (62322514), Anhui Science Fund for Distinguished Young Scholars
540 (2308085J25), and National Key Research and Development Program of China (2023YFC3709502,
541 2022YFC3700100).

542

543 **Financial support**

544 This work has been supported by Excellent Young Scientists Fund of the National Natural Science
545 Foundation of China (62322514), Anhui Science Fund for Distinguished Young Scholars

546 (2308085J25), and National Key Research and Development Program of China (2023YFC3709502,
547 2022YFC3700100).

548

549 **Author contributions**

550 HY and YWS designed this study. ZFP wrote the paper with help from HY and YWS. ZFP
551 contributed to analysis of the data for this study. All co-authors commented on this study.

552

553 **References**

554 China publishes action plan to improve air quality:
555 [https://english.www.gov.cn/policies/latestreleases/202312/08/content_WS65724f25c6d0868f4e8e](https://english.www.gov.cn/policies/latestreleases/202312/08/content_WS65724f25c6d0868f4e8e1fcb.html)
556 [1fcb.html](https://english.www.gov.cn/policies/latestreleases/202312/08/content_WS65724f25c6d0868f4e8e1fcb.html), last access: 16 May 2025.

557 Determination of atmospheric particles PM₁₀ and PM_{2.5} in ambient air by gravimetric method:
558 [https://english.mee.gov.cn/Resources/standards/Air_Environment/air_method/201111/t20111101_](https://english.mee.gov.cn/Resources/standards/Air_Environment/air_method/201111/t20111101_219390.shtml)
559 [219390.shtml](https://english.mee.gov.cn/Resources/standards/Air_Environment/air_method/201111/t20111101_219390.shtml), last access: 1 December 2025.

560 Multi-scale analysis of the impacts of meteorology and emissions on PM_{2.5} and O₃ trends at various
561 regions in China from 2013 to 2020 2. Key weather elements and emissions - ScienceDirect:
562 <https://www.sciencedirect.com/science/article/pii/S0048969722009391#s0030>, last access: 16 July
563 2025.

564 Specifications and Test Procedures for Ambient Air Quality Continuous Automated Monitoring
565 System for SO₂, NO₂, O₃ and CO:
566 [https://english.mee.gov.cn/Resources/standards/Air_Environment/air_method/201308/t20130816_](https://english.mee.gov.cn/Resources/standards/Air_Environment/air_method/201308/t20130816_257557.shtml)
567 [257557.shtml](https://english.mee.gov.cn/Resources/standards/Air_Environment/air_method/201308/t20130816_257557.shtml), last access: 1 December 2025.

568 Specifications and Test Procedures for PM₁₀ and PM_{2.5} Sampler:
569 [https://english.mee.gov.cn/Resources/standards/Air_Environment/air_method/201308/t20130816_](https://english.mee.gov.cn/Resources/standards/Air_Environment/air_method/201308/t20130816_257558.shtml)
570 [257558.shtml](https://english.mee.gov.cn/Resources/standards/Air_Environment/air_method/201308/t20130816_257558.shtml), last access: 1 December 2025.

571 The State Council rolls out a three-year action plan for clean air:
572 https://english.mee.gov.cn/News_service/news_release/201807/t20180713_446624.shtml, last
573 access: 16 May 2025.

574 WHO global air quality guidelines: particulate matter (PM_{2.5} and PM₁₀), ozone, nitrogen dioxide,
575 sulfur dioxide and carbon monoxide: <https://www.who.int/publications/i/item/9789240034228>, last
576 access: 6 May 2025.

577 Bian, L., Qin, X., Zhang, C., Guo, P., and Wu, H.: Application, interpretability and prediction of
578 machine learning method combined with LSTM and LightGBM-a case study for runoff simulation
579 in an arid area, *J. Hydrol.*, 625, 130091, <https://doi.org/10.1016/j.jhydrol.2023.130091>, 2023.

580 Chen, Y., Su, W., Xing, C., Yin, H., Lin, H., Zhang, C., Liu, H., Hu, Q., and Liu, C.: Kilometer-
581 level glyoxal retrieval via satellite for anthropogenic volatile organic compound emission source
582 and secondary organic aerosol formation identification, *Remote Sens. Environ.*, 270, 112852,
583 <https://doi.org/10.1016/j.rse.2021.112852>, 2022.

584 Dai, H., Zhu, J., Liao, H., Li, J., Liang, M., Yang, Y., and Yue, X.: Co-occurrence of ozone and
585 PM_{2.5} pollution in the Yangtze River Delta over 2013–2019: Spatiotemporal distribution and
586 meteorological conditions, *Atmospheric Res.*, 249, 105363,
587 <https://doi.org/10.1016/j.atmosres.2020.105363>, 2021.

588 Dai, H., Liao, H., Li, K., Yue, X., Yang, Y., Zhu, J., Jin, J., Li, B., and Jiang, X.: Composited
589 analyses of the chemical and physical characteristics of co-polluted days by ozone and PM_{2.5} over
590 2013–2020 in the Beijing–Tianjin–Hebei region, *Atmospheric Chem. Phys.*, 23, 23–39,
591 <https://doi.org/10.5194/acp-23-23-2023>, 2023.

592 Ding, A., Huang, X., Nie, W., Chi, X., Xu, Z., Zheng, L., Xu, Z., Xie, Y., Qi, X., Shen, Y., Sun, P.,
593 Wang, J., Wang, L., Sun, J., Yang, X.-Q., Qin, W., Zhang, X., Cheng, W., Liu, W., Pan, L., and Fu,
594 C.: Significant reduction of PM_{2.5} in eastern China due to regional-scale emission control: evidence
595 from SORPES in 2011–2018, *Atmospheric Chem. Phys.*, 19, 11791–11801,
596 <https://doi.org/10.5194/acp-19-11791-2019>, 2019.

597 Dominici, F., Greenstone, M., and Sunstein, C. R.: Particulate Matter Matters, *Science*, 344, 257–
598 259, <https://doi.org/10.1126/science.1247348>, 2014.

599 Feng, X., Tian, Y., Xue, Q., Song, D., Huang, F., and Feng, Y.: Measurement report: Spatiotemporal
600 and policy-related variations of PM_{2.5} composition and sources during 2015–2019 at multiple sites
601 in a Chinese megacity, *Atmospheric Chem. Phys.*, 21, 16219–16235, <https://doi.org/10.5194/acp-21-16219-2021>, 2021.

603 Franklin, M., Koutrakis, P., and Schwartz, P.: The role of particle composition on the association
604 between PM_{2.5} and mortality, *Epidemiol. Camb. Mass*, 19, 680–689,
605 <https://doi.org/10.1097/ede.0b013e3181812bb7>, 2008.

606 Fu, L., Guo, Y., Zhu, Q., Chen, Z., Yu, S., Xu, J., Tang, W., Wu, C., He, G., Hu, J., Zeng, F., Dong,
607 X., Yang, P., Lin, Z., Wu, F., Liu, T., and Ma, W.: Effects of long-term exposure to ambient fine
608 particulate matter and its specific components on blood pressure and hypertension incidence,
609 *Environ. Int.*, 184, 108464, <https://doi.org/10.1016/j.envint.2024.108464>, 2024.

610 Jerrett, M.: Atmospheric science: The death toll from air-pollution sources, *Nature*, 525, 330–331,
611 <https://doi.org/10.1038/525330a>, 2015.

612 Ke, G., Meng, Q., Finley, T., Wang, T., Chen, W., Ma, W., Ye, Q., and Liu, T.-Y.: LightGBM: A
613 Highly Efficient Gradient Boosting Decision Tree, in: *Advances in Neural Information Processing*
614 *Systems*, 2017.

615 Kioumourtzoglou, M.-A., Schwartz, J. D., Weisskopf, M. G., Melly, S. J., Wang, Y., Dominici, F.,
616 and Zanobetti, A.: Long-term PM_{2.5} Exposure and Neurological Hospital Admissions in the

617 Northeastern United States, *Environ. Health Perspect.*, 124, 23–29,
618 <https://doi.org/10.1289/ehp.1408973>, 2016.

619 Leung, D. M., Tai, A. P. K., Mickley, L. J., Moch, J. M., van Donkelaar, A., Shen, L., and Martin,
620 R. V.: Synoptic meteorological modes of variability for fine particulate matter (PM_{2.5}) air quality in
621 major metropolitan regions of China, *Atmospheric Chem. Phys.*, 18, 6733–6748,
622 <https://doi.org/10.5194/acp-18-6733-2018>, 2018.

623 Liu, C., Yang, Y., Wang, H., Ren, L., Wei, J., Wang, P., and Liao, H.: Influence of Spatial Dipole
624 Pattern in Asian Aerosol Changes on East Asian Summer Monsoon, *J. Clim.*, 36, 1575–1585,
625 <https://doi.org/10.1175/JCLI-D-22-0335.1>, 2023.

626 Peng, Z., Zhang, B., Wang, D., Niu, X., Sun, J., Xu, H., Cao, J., and Shen, Z.: Application of
627 machine learning in atmospheric pollution research: A state-of-art review, *Sci. Total Environ.*, 910,
628 168588, <https://doi.org/10.1016/j.scitotenv.2023.168588>, 2024.

629 Seaton, A., MacNee, W., Donaldson, K., and Godden, D.: Particulate air pollution and acute health
630 effects, *Lancet Lond. Engl.*, 345, 176–178, [https://doi.org/10.1016/s0140-6736\(95\)90173-6](https://doi.org/10.1016/s0140-6736(95)90173-6), 1995.

631 Shen, L., Mickley, L. J., and Murray, L. T.: Influence of 2000–2050 climate change on particulate
632 matter in the United States: results from a new statistical model, *Atmospheric Chem. Phys.*, 17,
633 4355–4367, <https://doi.org/10.5194/acp-17-4355-2017>, 2017.

634 Song, X.-H., Yan, L., Liu, W., He, J.-Y., Wang, Y.-C., Huang, T.-L., Li, Y.-Y., Chen, M., Meng,
635 J.-J., and Hou, Z.-F.: [Spatiotemporal Distribution Characteristics of Co-pollution of PM_{2.5} and
636 Ozone over BTH with Surrounding Area from 2015 to 2021], *Huan Jing Ke Xue Huanjing Kexue*,
637 44, 1841–1851, <https://doi.org/10.13227/j.hjcx.202205089>, 2023.

638 Sun, Y., Yin, H., Liu, C., Zhang, L., Cheng, Y., Palm, M., Notholt, J., Lu, X., Vigouroux, C., Zheng,
639 B., Wang, W., Jones, N., Shan, C., Qin, M., Tian, Y., Hu, Q., Meng, F., and Liu, J.: Mapping the
640 drivers of formaldehyde (HCHO) variability from 2015 to 2019 over eastern China: insights from
641 Fourier transform infrared observation and GEOS-Chem model simulation, *Atmospheric Chem.*
642 *Phys.*, 21, 6365–6387, <https://doi.org/10.5194/acp-21-6365-2021>, 2021a.

643 Sun, Y., Yin, H., Liu, C., Mahieu, E., Notholt, J., Té, Y., Lu, X., Palm, M., Wang, W., Shan, C., Hu,
644 Q., Qin, M., Tian, Y., and Zheng, B.: The reduction in C₂H₆ from 2015 to 2020 over Hefei, eastern
645 China, points to air quality improvement in China, *Atmospheric Chem. Phys.*, 21, 11759–11779,
646 <https://doi.org/10.5194/acp-21-11759-2021>, 2021b.

647 Tiwari, P., Cohen, J. B., Lu, L., Wang, S., Li, X., Guan, L., Liu, Z., Li, Z., and Qin, K.: Multi-
648 platform observations and constraints reveal overlooked urban sources of black carbon in Xuzhou
649 and Dhaka, *Commun. Earth Environ.*, 6, 38, <https://doi.org/10.1038/s43247-025-02012-x>, 2025.

650 Wang, S., Cohen, J. B., Deng, W., Qin, K., and Guo, J.: Using a New Top-Down Constrained
651 Emissions Inventory to Attribute the Previously Unknown Source of Extreme Aerosol Loadings
652 Observed Annually in the Monsoon Asia Free Troposphere, *Earths Future*, 9, e2021EF002167,
653 <https://doi.org/10.1029/2021EF002167>, 2021.

654 Wang, S., Cohen, J. B., Guan, L., Lu, L., Tiwari, P., and Qin, K.: Observationally constrained global
655 NO_x and CO emissions variability reveals sources which contribute significantly to CO₂ emissions,
656 *Npj Clim. Atmospheric Sci.*, 8, 87, <https://doi.org/10.1038/s41612-025-00977-2>, 2025.

657 Wang, X., Xue, Y., Jin, C., Sun, Y., and Li, N.: Spatial downscaling of surface ozone concentration
658 calculation from remotely sensed data based on mutual information, *Front. Environ. Sci.*, 10,
659 <https://doi.org/10.3389/fenvs.2022.925979>, 2022.

660 Wu, P.-C. and Huang, K.-F.: Tracing local sources and long-range transport of PM₁₀ in central
661 Taiwan by using chemical characteristics and Pb isotope ratios, *Sci. Rep.*, 11, 7593,
662 <https://doi.org/10.1038/s41598-021-87051-y>, 2021.

663 Yin, H., Sun, Y., Liu, C., Zhang, L., Lu, X., Wang, W., Shan, C., Hu, Q., Tian, Y., Zhang, C., Su,
664 W., Zhang, H., Palm, M., Notholt, J., and Liu, J.: FTIR time series of stratospheric NO₂ over Hefei,
665 China, and comparisons with OMI and GEOS-Chem model data, *Opt. Express*, 27, A1225–A1240,
666 <https://doi.org/10.1364/OE.27.0A1225>, 2019.

667 Yin, H., Sun, Y., Liu, C., Lu, X., Smale, D., Blumenstock, T., Nagahama, T., Wang, W., Tian, Y.,
668 Hu, Q., Shan, C., Zhang, H., and Liu, J.: Ground-based FTIR observation of hydrogen chloride (HCl)
669 over Hefei, China, and comparisons with GEOS-Chem model data and other ground-based FTIR
670 stations data, *Opt. Express*, 28, 8041–8055, <https://doi.org/10.1364/OE.384377>, 2020.

671 Yin, H., Sun, Y., Wang, W., Shan, C., Tian, Y., and Liu, C.: Ground-based high-resolution remote
672 sensing of sulphur hexafluoride (SF₆) over Hefei, China: characterization, optical misalignment,
673 influence, and variability, *Opt. Express*, 29, 34051–34065, <https://doi.org/10.1364/OE.440193>,
674 2021a.

675 Yin, H., Liu, C., Hu, Q., Liu, T., Wang, S., Gao, M., Xu, S., Zhang, C., and Su, W.: Opposite impact
676 of emission reduction during the COVID-19 lockdown period on the surface concentrations of
677 PM_{2.5} and O₃ in Wuhan, China, *Environ. Pollut.*, 289, 117899,
678 <https://doi.org/10.1016/j.envpol.2021.117899>, 2021b.

679 Yin, H., Lu, X., Sun, Y., Li, K., Gao, M., Zheng, B., and Liu, C.: Unprecedented decline in
680 summertime surface ozone over eastern China in 2020 comparably attributable to anthropogenic
681 emission reductions and meteorology, *Environ. Res. Lett.*, 16, 124069,
682 <https://doi.org/10.1088/1748-9326/ac3e22>, 2021c.

683 Yin, H., Sun, Y., Notholt, J., Palm, M., Ye, C., and Liu, C.: Quantifying the drivers of surface ozone
684 anomalies in the urban areas over the Qinghai-Tibet Plateau, *Atmospheric Chem. Phys.*, 22, 14401–
685 14419, <https://doi.org/10.5194/acp-22-14401-2022>, 2022a.

686 Yin, H., Sun, Y., You, Y., Notholt, J., Palm, M., Wang, W., Shan, C., and Liu, C.: Using machine
687 learning approach to reproduce the measured feature and understand the model-to-measurement
688 discrepancy of atmospheric formaldehyde, *Sci. Total Environ.*, 851, 158271,
689 <https://doi.org/10.1016/j.scitotenv.2022.158271>, 2022b.

690 Zhang, H., Si, S., and Hsieh, C.-J.: GPU-acceleration for Large-scale Tree Boosting,

691 <https://doi.org/10.48550/arXiv.1706.08359>, 26 June 2017.

692 Zhang, Q., Meng, X., Shi, S., Kan, L., Chen, R., and Kan, H.: Overview of particulate air pollution
693 and human health in China: Evidence, challenges, and opportunities, *The Innovation*, 3, 100312,
694 <https://doi.org/10.1016/j.xinn.2022.100312>, 2022a.

695 Zhang, R., Wang, G., Guo, S., Zamora, M. L., Ying, Q., Lin, Y., Wang, W., Hu, M., and Wang, Y.:
696 Formation of urban fine particulate matter, *Chem. Rev.*, 115, 3803–3855,
697 <https://doi.org/10.1021/acs.chemrev.5b00067>, 2015.

698 Zhang, Y., Yu, S., Chen, X., Li, Z., Li, M., Song, Z., Liu, W., Li, P., Zhang, X., Lichtfouse, E., and
699 Rosenfeld, D.: Local production, downward and regional transport aggravated surface ozone
700 pollution during the historical orange-alert large-scale ozone episode in eastern China, *Environ.*
701 *Chem. Lett.*, 20, 1577–1588, <https://doi.org/10.1007/s10311-022-01421-0>, 2022b.

702 Zhao, R., Gu, X., Xue, B., Zhang, J., and Ren, W.: Short period PM_{2.5} prediction based on
703 multivariate linear regression model, *PLOS ONE*, 13, e0201011,
704 <https://doi.org/10.1371/journal.pone.0201011>, 2018.

705 Zhao, X. J., Zhao, P. S., Xu, J., Meng, Pu, W. W., Dong, F., He, D., and Shi, Q. F.: Analysis of a
706 winter regional haze event and its formation mechanism in the North China Plain, *Atmospheric*
707 *Chem. Phys.*, 13, 5685–5696, <https://doi.org/10.5194/acp-13-5685-2013>, 2013.

708